Nanogenerator-Based Bidirectional Pressure Sensor Array and Its Demonstration in Underwater Invasive Species Detection

Yunqi Cao[1], Hongyang Shi[2], Xiaobo Tan[2] and Nelson Sepúlveda[2*]

Just Accepted

This is a "Just Accepted" manuscript, which has been examined by the peer-review process and has been accepted for publication. A "Just Accepted" manuscript is published online shortly after its acceptance,which is prior to technical editing and formatting and author proofing. Tsinghua University Press (TUP) provides "Just Accepted" as an optional and free service which allows authors to make their results available to the research community as soon as possible after acceptance. After a manuscript has been technically edited and formatted, it will be removed from the "Just Accepted" Web site and published as an ASAP article. Please note that technical editing may introduce minor changes to the manuscript text and/or graphics which may affect the content, and all legal disclaimers that apply to the journal pertain. In no event shall TUP be held responsible for errors or consequences arising from the use of any information contained in these "Just Accepted" manuscripts. To cite this anuscript please use its Digital Object Identifier (DOI®),which is identical for all formats of publication.

Address correspondence to First A. Firstauthor, email1; Third C. Thirdauthor, email2

Nanogenerator-Based Bidirectional Pressure Sensor Array and Its Demonstration in Underwater Invasive Species Detection

Yunqi Cao[1], Hongyang Shi[2], Xiaobo Tan[2] and Nelson Sepúlveda[2]*

[1]State Key Laboratory of Industrial Control Technology, College of Control Science and Engineering, Zhejiang University, Hangzhou, Zhejiang 310027, China

[2]Department of Electrical and Computer Engineering, Michigan State University, East Lansing, Michigan 48824, United States

Abstract

Assessment of spawning-phase dynamics is an essential prerequisite to successful control of invasive sea lampreys in Great Lakes areas, which cause in catastrophic damages in both commercial fishery and ecological systems. However, current assessment strategies may pose challenges for lake-wide abundance estimation and non-target anadromous species preservation. Here, we demonstrate an efficacious species-specific non-destructive sensing system based on porous ferroelectret nanogenerator for *in-situ* monitoring of lamprey spawning migration using their unique suction behavior. Simulations show that the porous structure enables a redistribution of surface charges under bidirectional deformations, which allows the detection of both positive and negative pressures. The quasi-piezoelectric effect is further validated by quantitative analysis in a wide pressure range of -50 to 60 kPa, providing detailed insights into transduction working principles. For reliable lamprey detection, a 4×4-pixel sensor array is developed and integrated with a complementary metal-oxide-semiconductor (CMOS) based signal processing array thus constituting a sensing panel capable of recording oral suction patterns in an underwater environment.

Figure for TOC
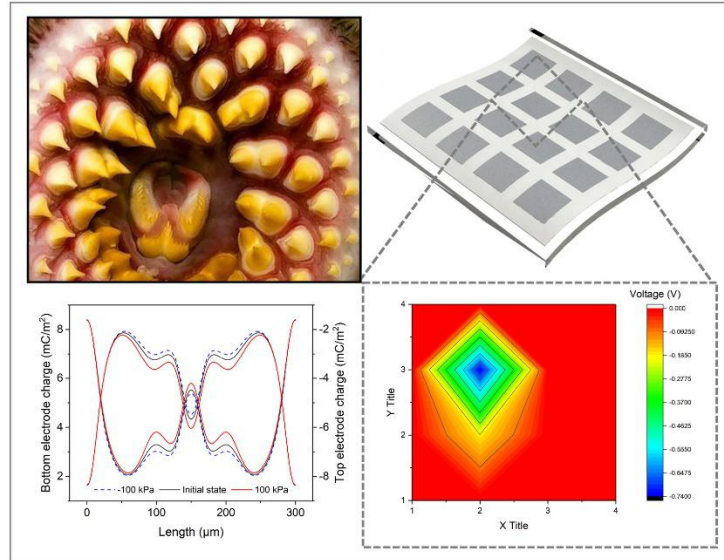
Introduction

Sea lamprey (Petromyzon marinus), an anadromous fish native to the Atlantic Ocean, first invaded Laurentian Great Lakes in the early 1900s and rapidly spread throughout the water bodies of the Great Lakes region [1]. Though controversy remains on their origin in Lake Ontario [2], the booming population has resulted in a catastrophic reduction in the abundance of economically and ecologically important species, such as lake trout and whitefish [3], posing a grave threat to commercial fish harvest as well to the biodiversity of the freshwater ecosystem [4][5]. An extensive control program dedicated to reducing the lamprey population below economic injury level (EIL) has been carried out for decades and demonstrated remarkable progress in saving economic losses [6][7]. Prior to more cost-effective control action, the development of efficacious population assessment methods that target different life stages (including distinct spawning, parasitic, metamorphosis, and larval phases) is imperative [8]. Particularly, spawning-phase assessment as an essential component of the integrated management, could considerably

advance our understanding of sea lamprey migration timing and population dynamics, and the development of regression models for whole-lake relative abundance estimation [8][9].

As the most predominant assessment method, spawning run size can be estimated by mark-recapture at release locations [10]. However, a significant amount of effort needs to be dedicated, making widespread deployment rather difficult and surveillance database limited to a few tributaries [11]. Besides, its interference in migrating behavior, though less disruptive compared to trapping operation, inevitably induces uncertainties to extrapolated lake-wide estimation. Molecular surveillance, which evaluates environmental DNA (eDNA) introduced by the decomposition of dead lamprey organisms, has been demonstrated as an emerging non-destructive technique for species-specific monitoring [12][13]. This method can effectively alleviate the pain of intensive fieldwork, refine the control methods, and perform early detection in new water bodies [12]. Despite many merits, the implementation of the eDNA approach is subject to physical environmental challenges, such as water temperature variation, degradation of organisms, and dilution [12][14], which could result in low accuracy of interpretation. Therefore, a more reliable, species-specific, and non-disruptive monitoring method is of great interest to spawning lamprey assessment. One unique behavior of spawning lampreys that distinguishes them from other anadromous fishes is the use of oral suction pressure (the same mechanism they use to predate other fish) to frequently hold their positions under fast-flowing current to conserve energy for intermittent high-speed upstream swimming [15]. Since the lampreys are more inclined to suck on flat rock surfaces [16], it is reasonable to develop a pressure sensing panel that can be deployed in tributaries and to *in-situ* collect dynamic information on the lamprey population. Such detection systems based on suction behaviors have recently been proposed but have yet to be thoroughly investigated [17-19].

The biggest obstacle that impedes the implementation of suction-based assessment is developing a sensing panel capable of detecting both compression (positive pressure) and partial vacuum (negative pressure) in a field environment. Although positive pressure sensing has been well studied, the detection of negative pressure using the same transduction mechanism remains problematic due to the visco-elasticity of substrate material, which makes the sensor insensitive to negative pressures [20]. Micro-

3

structured flexible sensors can in theory respond to bidirectional pressures [21], but most micro-structures, such as micro-pillar [22], micro-dome [23], and micro-pyramid [24][25], are dedicated to improving sensitivities for positive pressure sensors only. The lack of proper bonding and encapsulation process causes easy delamination under negative pressures and failure in underwater applications, thus micro-structure with sealed air cavities is indispensable for such practices. Piezoresistive pressure sensors based on deformable Parylene-C supporting membranes and vertically aligned carbon nanotubes (CNTs) were developed for pressure sensing in the range of -50 to 50 kPa [26], but the high-temperature coefficient of resistance (TCR) for CNTs may cause ambiguity in a complex environment. Another research has demonstrated a capacitive pressure sensor consisting of Ecoflex-0030 dielectric layers with embedded air gap channels to observe 2.63 times improvement in sensitivity and measure both positive and negative pressure distributions [20]. Unfortunately, the low baseline capacitance makes the sensing system vulnerable to bio-electromagnetic interference [27][28] caused by animal approaching and failing to detect sea lampreys in an underwater environment. Similarly, sealed air cavities can also be found in ferroelectret nanogenerators (FENGs) with porous structure [29][30], which not only deforms easily under positive pressures but also presumably responds to negative pressures due to the micro-cavity structure [31]. Such deformations can then be converted into electric signals based on the quasi-piezoelectric effect. Moreover, its fully integrated structure with high mechanical strength and waterproofness [32] provides more robustness for underwater animal detection. Nevertheless, simultaneous detection of both positive and negative pressures using nanogenerator-based pressure sensors has not been demonstrated and is worth exploiting in lamprey assessment practices.

Here, an assessment strategy that exploits the characteristic suction behavior of spawning-phase (adult) sea lamprey is proposed. The presented nanogenerator-based pressure sensor array demonstrates bidirectional pressure sensing ability that can convert mechanical stimuli into electrical signals under both positive and negative pressures. The mechanoelectrical transduction mechanism is studied analytically and experimentally in detail. It has been found that the porous structure is the most critical attribute to enabling negative pressure sensing and meanwhile improves sensitivity, whereas the solid top and bottom

polypropylene (PP) layers are of great importance in underwater sensing applications. The combination of a pressure sensor array and a transistor-based signal processing array is used to extend the measuring time, which allows a more robust assessment of the sea lamprey suction event during a full attach-detach cycle. However, continuous monitoring of static pressure is still difficult due to the nature of the piezoelectric effect. Therefore, the presented work aims at recognizing the lamprey-specific footprint in an underwater environment rather than suction dynamics information, demonstrating a promising approach for in situ monitoring of spawning migration of sea lampreys in the Great Lakes. The developed sensing devices can be widely distributed in tributary systems to not only enumerate the abundance of spawning adult lampreys but also accurately determine the spawning locations and timing, providing a more efficient field study method to better understand sea lamprey migration timing and further assist sea lampreys control efforts such as the deployment of traps [33] and seasonal barriers [34]. It can also be used at strategically chosen locations (such as fishways) to trigger lamprey control actions (e.g., deterrence or capture, and fishway operation).

Results

Device structure. The multilayer FENG device consists of a polypropylene ferroelectret (PPFE) layer with two metal thin films as top and bottom electrodes. Fig. 1a shows a cross-sectional scanning electron microscopy (SEM) observation of the pressure-sensitive PPFE film, where the total thickness of the PPFE film is approximately 80 µm, which consists of a 40 µm porous middle region between two 20 µm denser layers. The preparation of the PPFE film starts with a PP film dispersed with silicate nanoparticles as stress raisers (details in Supplementary Fig. 1). During the in-plane bidirectional stretching process, micro-cracks occur once the concentrated normal stress exceeds the material stress limit and develops along tensile directions. A high-pressure nitrogen environment is introduced to allow gas molecules to diffuse into the film, and then the high-pressure atmosphere is suddenly released to allow micro-cracks to expand into ellipsoid voids with elliptic radii ranging from 1 to 50 µm. After the thermal stabilization of the structure, a high electric field is applied to break gas molecules into plasma, leading to the upper and

lower surfaces of each void being oppositely charged. Finally, the metallization of electrodes is completed by sputter coating of two 500 nm silver layers on both top and bottom surfaces of the PPFE film with the assistance of a shadow mask. Fig. 1b,c show close-up views of the solid and the ellipsoid structures, respectively. Top-view SEM images using secondary and backscattered electron contrast are also shown in Fig. 1d,e to further reveal the internal microstructure of the PPFE film. The schematics of the macro dipoles and their responses under positive and negative pressures are also shown in Fig. 2 and Supplementary Fig. 2 in order to have a more straightforward understanding of the internal microstructures and the working principles. Because the production of backscattered electrons is strongly correlated to the density of the interaction volume, the internal ellipsoid voids are indicated by those darker regions while the silicate nanoparticles appear much brighter than the surrounding medium. It can be clearly seen that the two solid layers of the PPFE film naturally encapsulate the piezoelectric active layer and consequently prevents the potential water-induced sensor performance degradation as demonstrated in our previous work [32].

Transduction mechanisms under positive and negative pressures. This section describes the mechanoelectrical transduction process of FENG under both positive and negative pressures. In the initial condition, as shown in Fig. 2a, trapped charges created by plasma discharge are localized on both upper and lower surfaces of the micro-voids due to electric field poling. The oppositely charged air-void surfaces form micrometer-sized dipole moments, which contribute to spontaneous polarization in the through-thickness direction and induce ferroelectricity. Therefore, surface charge density is induced on the lower and upper surfaces of the top and bottom solid PP layers, respectively, due to the polarization field originating from the middle porous layer. Consequently, induced charge density (σ_e) that opposes the polarity of σ_p, due to electrostatic induction, accumulates at the Ag/PP interfaces on top and bottom surfaces (Supplementary Fig. 2). When a positive pressure load is applied to the surface side with negatively charged σ_e, the dipole moments decrease in magnitude and thus lead to an increase of positive

charges on this negatively charged surface. The redistribution of σ_e generates a potential difference that outputs an electric signal as shown in Fig. 2b. Similarly, during the unloading stage as illustrated in Fig. 2c, electric output with opposite polarity can be expected due to the reversion process of electric dipole moments. In short, the mechanoelectrical transduction is enabled first by the mechanical response of charged air voids under external pressures, and then by the surface charge redistribution due to the consequent polarization field reconstruction. Air-voided structures are often used in polymer-based pressure sensors to reduce viscoelasticity, which not only efficiently reduces the hysteresis effect but also facilitates the large deformation under negative pressures (vacuum forces). Therefore, it is reasonable to deduce that the FENG is capable of negative pressure sensing and the electric output shows behaviors opposite to those under positive pressures as described in Fig. 2d,e. The finite element method (FEM) simulation is carried out to further investigate the energy conversion process during mechanical-to-electrical transduction. Fig. 2f,g present the distribution of σ_e on both top and bottom PP layers under positive and negative pressures compared to the initial state for devices with and without middle layer porous structure, respectively. It is obvious that, for the electrical connections described in Fig. 2a-e, positive charges accumulate at the top and bottom surfaces, respectively, due to positive and negative pressures while negative charges accumulate on the other surface sides under the same pressure type. Besides, the porous structure is also found to be of great importance to pressure sensing, especially for negative pressures. Fig. 2h shows the converted electrical energy due to surface charge accumulation. In addition to the negative pressure sensing, the porous structure significantly increases the sensitivity in both positive and negative pressure sensing.

Device operation for positive and negative pressures. To study the mechanoelectrical transduction behavior in FENG-based pressure sensors, open-circuit voltage (V_{oc}) and short-circuit current (I_{sc}) measurements were performed on a 9 mm $\times$ 9 mm single sensing element, which represents an individual sensing pixel element of a 4 $\times$ 4 sensor array (see Fig. 4b), under both positive and negative

pressures. It is worth mentioning that the device characterizations under both positive and negative pressures were performed on the pressure sensing panel used for the underwater animal test, where the schematic drawing of the sensing panel is shown in Fig. 3a and Fig. 3d. Fig. 3a shows the schematic illustration of the experimental setup that was used for device characterizations under positive pressures. The positive pressure was generated by using a customized computer-controlled linear actuator to modulate the traveling distances and speeds of a rubber indenter, to induce compressive stress cycles. The applied pressure levels were monitored by a flexible force sensor placed between the indenter and the PDMS layer encapsulating the sensing panel. Fig. 3b shows the time-domain V_{oc} output signals of a single-pixel FENG under various pressure amplitudes at the same loading rate of -140 kPa/s, with V_{oc} peak values increasing monotonically with the amplitude of the applied pressures. It is worth mentioning that the V_{oc} represents the linear coupling between applied pressures and the polarization field. Therefore, unlike I_{sc} that exhibits positive and negative poles, V_{oc} only exhibits unidirectional peaks under pure positive or negative pressure inputs. This phenomenon can also be found in triboelectric nanogenerator (TENG) based pressure sensors [35-39]. However, when a low-impedance measuring instrument is used, the voltage output shows a pair of positive and negative spikes [40] and cannot be considered as V_{oc}. The underlying physics of this impedance-dependent voltage measurement can be found in our previous work [41]. Comparing the inset of Fig. 3b and Fig. 3g (top), it can be noticed how the V_{oc} increases during the loading stage and decreases during the releasing stage, which represents the direct coupling between the mechanical and the electrical domains. It should be noted that the pixelated electrodes were patterned on the surface side with positively charged σ_e (opposite to the orientation as demonstrated in Fig. 2), leading to negative V_{oc} outputs under positive pressures; which is opposite of what has been reported in previous works [41-44]. Fig. 3c shows the I_{sc} output under positive pressures with loading rates of -45 kPa/s, -88 kPa/s, and -140 kPa/s under the same magnitude of 56 kPa. The magnitude of I_{sc} increases with the loading rate, with a negative/positive sign for the loading/releasing stages, respectively. Since the applied pressure causes a time-varying electric field, this dependency of I_{sc} on the loading rate is indicative that

the measured charge flow originates from the displacement current, i.e. $I_{sc} = A \cdot \partial D / \partial t$, where A is the area of the contact area, D is the electric displacement, and t is time. It is not surprising that the FENG shows a strong quasi-piezoelectric effect under positive loads. However, its mechanoelectrical response under negative pressures has not been exploited yet. As shown in Fig. 3d, the negative pressures used in this experiment were created via a soft suction cup, which is driven by a pneumatic fluidic control system (Supplementary Fig. 3) consisting of a vacuum pump, a solenoid value, a vacuum sensor, and a microcontroller. The behaviors of V_{oc} and I_{sc} under negative pressures were measured and presented in Fig. 3e,f respectively, while the amplitudes of V_{oc} and I_{sc} as function of pressures ranging from -50 to 60 kPa with various loading rates are presented in Fig. 3h,i. Results in Fig. 3h show the V_{oc} peak changing from -0.16 to -27.12 V as the pressure amplitude increases from 7 to 56 kPa, while for negative pressures, the V_{oc} peak was 16.54 V under -49 kPa --which is about 39% lower than the output under 56 kPa. The V_{oc} output is found to be mainly dependent on the loading amplitude, but not very sensitive to the loading rates. It should be noted that the generation of V_{oc} relies on the σ_e accumulation as demonstrated in Fig. 2. Thus, the internal resistance of the testing device creates a path for discharging of σ_e, which results in a lower measured V_{oc}. Another difference between the positive and negative pressure experiments studied in this work is that the response of the latter is likely to include high-frequency responses from the vibrations produced by the mechanical pump used to generate negative pressures, which could be transmitted to the device through the suction cup. A high-frequency component in the loading pressure could be generating the large negative spikes in Fig. 3f. The absence of these vibrations for positive pressure experiments is likely to be responsible for the smaller gaps between the three curves. The quasi-piezoelectric effect of FENG is confirmed in Fig. 3i, where the current amplitude shows dependency on the rate of the applied pressure for both positive and negative pressures. It is worth noting that, for any given loading rate, when comparing pressures of the same amplitude but a different sign, the magnitude of I_{sc} is consistently smaller for the negative pressure input. However, the fluctuations (or spikes) observed for I_{sc} for negative pressures complicates the measurement of the I_{sc} magnitude, especially for

small negative pressures with lower loading rates, where the magnitude of the spike is much larger than the rest of the current generated during the cycle. We believe that this is the reason for the overlapping data points in the ±45 kPa/s and ±88 kPa/s I_{sc} curves at -10 kPa (see Fig. 3i). Although the measured electric output (V_{oc} and I_{sc}) under negative pressures share similar patterns as demonstrated under positive pressures shown in Fig. 3b,c, it is evident that their responsivity is lower for the negative pressures. This observation is supported by the FEM results as shown in Fig. 2h, and a physical explanation can be given in terms of material properties and acting forces under an applied negative pressure. During the device fabrication, the expansion of air voids may cause structural deformation beyond the linearity limit in the stress-strain curve (i.e. material reaches the plastic deformation region). For most materials, the induced stress per unit strain is significantly reduced outside the elastic region -in fact, it could even become negative, leading to a lower responsivity during tensile and compressive loading tests. Additionally, after the device is fabricated, any mechanical expansion of the film along its thickness (which is expected to occur due to a negative pressure input) would experience a counter electrostatic force between the top and bottom electrodes, caused by the accumulated charges of opposite polarity on each surface.

System Integration: Combining sensor with CMOS-based readout circuit. Dynamic pressure sensing using piezoelectric-based tactile sensors is widely adopted for applications such as human-machine interaction and human motion monitoring due to the advantages of short response time, wide frequency range, and good linearity [45][46]. Generally, monitoring mechanical phenomena requires transduction of force and displacement into electrostatic potential (i.e. voltage) and/or charge flow (i.e. current). Using a FENG device (or any device based on the same piezoelectric principle) as a transduction mechanism provides both electrical signals in response to a mechanical input, but its main advantage is that such devices enable the characterization of the magnitude and dynamic behavior of the forces and displacements. As explained previously, the I_{sc} generated by the FENG device is proportional to the

loading rate of the applied pressure, and therefore, such a signal is better used for describing the dynamic mechanical behavior, especially when high-frequency environmental fluctuations are of high interest. V_{oc}, on the other hand, is linearly dependent on the magnitude of the applied pressure, but the loading rate can also be extracted from its output waveform. However, accurate measurement of the V_{oc} waveform requires extra circuitry to match the impedance of the device and the instrument, which increases the system complexity and does not provide a holistic approach that can be implemented universally in systems that use any form of piezoelectric transduction. A solution to this problem is found through the integration of the piezoelectric sensing element with the gate terminal of a metal–oxide–semiconductor field emission transistor (MOSFET), where the channel conductance can be modulated by the stress-induced charge accumulation. The output signal in terms of the drain current (I_{DS}) not only ensures a better signal-to-noise ratio [47] in the underwater environment but also considerably extends static pressure measuring time, which allows the sensing system to have enough time to sequentially scan individual pixels without missing important diagnostic information. This becomes even more favorable for cases where the mechanical input consists of positive and negative pressures, as in the present target application of sea lamprey detection. A characteristic pressure mapping of sea lamprey attachment contains a negative pressure center area generated by the suction and a surrounding positive pressure area due to the compression of the mouth rim. Therefore, each sensing element needs to have the ability to differentiate between positive and negative pressures, which is accomplished by the approach used in the present work. As shown in Fig. 4a, a specific sensing strategy is implemented by integrating the FENG with a complementary MOSFET (CMOSFET/CMOS)-based charge amplifier unit, where the FENG electrode with positively charged σ_e surface is electrically wired to the commonly connected gates G$_1$ and G$_2$. In this case, when positive pressure is applied, a negative voltage is generated and supplied to both G$_1$ and G$_2$, which turns "on" the p-channel MOSFET, while the n-channel one remains "off". This generates a current flow I_F across the load resistor (R_l) and produces a positive output voltage V_{out}. Conversely, a negative pressure will produce a negative V_{out}.

Performance of the FENG-based pixelated sensor array. The complete sensing system consists of a

FENG-based sensor and a CMOS array, as shown in Fig. 4b. Each FENG sensing pixel element is

electrically connected to a CMOS-based charge amplifier unit, as described in Fig. 4a. V_{out} is measured

by a real-time controller (cRIO-9075, National Instruments) embedded with voltage input modules (NI-

9201, National Instruments) through fast switching among analog input channels that sequentially scans

each individual FENG/CMOS sensing pair. The V_{out} measurement of individual sensing elements under

cyclic pressure loads with various loading rates and loading amplitudes at different fixed V_{DD} values are

evaluated in Fig. 4c-e. The pixelated sensor array in the proposed sensing system also effectively limits

the cross-talk effect under positive and negative pressures as shown in Supplementary Fig. 4, which

provides the basis for accurate pressure mapping.} In order to turn the MOSFET "on", $|V_{GS}| = |V_G -$

$V_{DD}|$ must be greater than the threshold voltage $|V_{th}|$, where V_G is the gate voltage determined by the

electric field created by the transferred charge Q_t from the FENG device. Comparing Fig. 4c with Fig.

4d,e, we can see that the threshold pressure P_{th} decreases with higher V_{DD} for the transistor to be turned

on, since less transferred charges Q_t are required to flow into the gate terminal with the same gate

capacitance in order to reach the threshold voltage V_{th}. From the positive detection experiments shown in

Fig. 4c-e, it can be observed that the Q_t is only dependent on the pressure amplitude and independent of

the loading rate (which is in agreement with previous observations [42]), and that the loading rate seems

to have a great impact on P_{th} under negative pressures. This observation is explained by the lower

electromechanical response under negative pressures and the discharging of the effective capacitance

between the gate and source. While a certain pressure load is being applied to the FENG, the $|V_{GS}|$

increases due to charge accumulation, but at the same time, the accumulated voltage at the gate terminal

will also be discharged through the internal resistance of the device. This process is similar to the

discharge of a voltage stored in a capacitor once it is connected to a load resistor. Thus, the discharging

problem is negligible for a fast pressure loading process, and lower P_{th} values can be detected, but the

problem is more prominent for the negative pressure sensing. The influence of V_{DD} on V_{out} under

different loading amplitudes and rates is assessed in Fig. 4f-h. Similarly, by increasing either the loading rate or V_{DD}, the P_{th} would be lowered especially under negative pressures. For example, in Fig. 4g, the P_{th} for positive pressure detection is around 23 kPa while the minimum detectable negative pressure is approximately -37 kPa at the same V_{DD} value of 0.4 V. When the V_{DD} is increased to 1.0 V, the P_{th} decreases to 20 kPa and -16 kPa, respectively. It should also be noted that although only one of the two transistors can be turned on at the same time, both gate terminals G₁ and G₂ are being charged when either a positive or negative pressure is detected, resulting in less charge flow into the effective transistor terminal than the total charge generated by the FENG (Q_t). Thus, the minimum detectable pressure in this configuration is higher than when using V_{oc} as the output signal -- see Fig. 3h. Thus, the threshold pressure induces a dead zone with no voltage output from about -10 to 20 kPa, imposing certain challenges in the determination of small suction pressures. However, the sensing ability of the proposed system is enough to detect the attachment of an adult sea lamprey, which exhibits a typical suction pressure in the range of -20 to -70 kPa [17]. Besides, for the purpose of lamprey assessment, it is preferable to have a detection system with more reliability in recognizing the suction pattern than knowing the exact pressure levels. On this basis, the proposed sensing system can reject small pressure inputs, which might be caused by environmental noises, and stay activated as long as the lamprey is attached to the sensing panel, making the sensing system more species-specific and capable of monitoring the full attach-to-detach process of sea lamprey as demonstrated in the next section.

Underwater detection of invasive sea lampreys. In order to validate the feasibility of implementing the proposed sensing technique in invasive lamprey migration assessment, experimental tests on adult lampreys were conducted at the Hammond Bay Biological Station of U.S. Geological Survey (USGS), Millersburg, Michigan, USA. All experimental procedures were under the protocols and guidelines approved by the Institutional Animal Care and Use Committee (IACUC) of Michigan State University, No. 02/18-028-00. Fig. 5a shows a close-up view of the disc-shaped mouth of the tested adult lamprey, and a top view photo showing its entire body, with its mouth attaching to a 4 × 4-pixel sensing panel

(more details in Supplementary Fig. 5). This setting emulates adult lampreys holding their positions during upstream migrating. It should be mentioned that the oral disks are developed when larval sea lampreys begin a dramatic metamorphosis towards the transforming phase. Therefore, lampreys' suction behavior persists during most of their lifespan (see Fig. 5b). Their attachment process does not involve a constant, static pressure. Instead, the process involves a series of intermittent cycles of fast pumping actions [17]. Thus, each pumping action supplies charge to the gate capacitance C_g, and consecutive operations lead to an accumulation of charge, which increases V_{GS} beyond the threshold voltage. As long as the lamprey stays attached to the sensing panel, charges are intermittently generated by the FENG, which not only suppresses the gate leakage current but also maintains V_{GS} at high levels. Although bidirectional dynamic pressure sensing can be achieved without CMOS integration as demonstrated in Fig. 3, such integration allows for detecting signals generated by either positive or negative pressures, which is required for some applications. In the particular case of sea lamprey detection, not being able to distinguish positive and negative pressures could lead to false reading signals from other marine animals such as the "white sucker" [48]. Therefore, we use a series of pumping actions as the species-specific biological footprint to improve the detection reliability and accuracy for future field deployment in monitoring spawning lampreys. Fig. 5c shows the voltage output (V_{DD}) of each individual sensing element (E_{ij}; $1 \leq i, j \leq 4$) during a complete attach-detach cycle observed from the underwater sensing panel. It can be seen that the voltage of E_{22} (which is located at the center of the suction area) gradually increases to the value of V_{DD} due to the accumulation of rapid pumping action and is maintained while the lamprey is attached during the time period region S_4 in the plot. Spatial mapping of pressure distribution is presented in Fig. 5d, showing the evolution of the suction pattern throughout time periods S_1 to S_6. It is worth noting that the positive pressures can only be generated on the edges of the oral disc upon physical contact, thus limiting the charge that can be produced from this small effective area [49]. Additionally, the same sensing unit is also partially under negative pressure, which produces a combination of positive and negative pressures exerted on the same sensor, resulting in net neutralization of output charges.

Supplementary Fig. 6 shows a simultaneous detection of both positive and negative pressures using a suction cup with a broader rim. The pressure distribution of adult sea lampreys attaching to different locations of the sensing panel is also shown in the supplementary Fig. 7, where the negative voltage indicates the characteristic negative pressure generated by the lamprey's suction behavior. In order to observe both positive and negative pressures on the same heat map, and to achieve a more photographic suction pressure pattern with a larger dynamic pressure sensing range, a sensor array with a pixel size smaller than the width of the mouth rim needs to be developed and integrated with a low C_g thin-film transistor (TFT) array [50] with lower turn-on voltage. In this way, the dead zone of zero voltage output as shown in Fig. 4 can be possibly narrowed or eliminated, leading to more accurate pressure measurement. Nevertheless, the proposed sensing panel with the current spatial resolution is capable of capturing the lamprey-specific biological footprint in an underwater environment, which provides insights into the distributed sensor network for non-destructive *in-situ* detection of spawning lampreys.

Discussion

In this study, we present a bidirectional pressure sensor array based on the combination of FENG and transistors for detecting both positive and negative pressures, enabling a novel, non-destructive technique for assessing spawning invasive spawning lampreys in an underwater environment. The pressure-sensitive FENG material consists of top and bottom solid PP layers, and a porous middle layer which plays a crucial role in both positive and negative pressure sensing. The deformation of film structure under external pressure loading causes a reconstruction of the polarization field, which consequently redistributes surface charges and generates an electric output signal with polarities depending on the types of applied pressures. Experimental characterizations further validate the direct piezoelectric effect, revealing the dependency of V_{oc} and I_{sc} on both pressures loading magnitude and rate. By integrating the FENG-based sensor array with a transistor-based signal processing array, the output charges can be

supplied simultaneously to both gate terminals and modify the channel conductance with either positive or negative pressure applied. This sensing configuration detects the complete attach-detach cycle as the lamprey-specific biological footprint rather than individual pressure pulses in terms of V_{DD} output, which provides more reliable assessment information. It should be noted that the purpose of using such a pressure-based lamprey detection technique is not to recognize every lamprey passing through the deployment location since it is not guaranteed that the lamprey will suck on the sensing panel, but once the unique negative and positive suction pattern is captured, the population dynamic information is obtained by knowing the parasitic sea lampreys have intruded this tributary. For a more reliable assessment, the proposed sensing technique may be enhanced by using pheromones [51] to attract migratory lampreys to suck on the sensing panel. Another concern for implementing this sensing technique in field deployment comes from arraying single sensing units on a large scale. For an M × N-pixel sensing panel, the current configuration requires M × N electrodes in order to have a crosstalk-free pressure distribution. However, the growing number of electrodes and wires significantly complicates the circuitry and the whole sensing system. In future work, we will consider using a recently developed crosstalk-free "row + column" electrodes [52] as the pressure sensing panel and including only one CMOS unit with the help of multiplexers. In this case, the total number of electrodes can be reduced to M + N. Nevertheless, the sensing system described in this work may pave the wave for in-situ assessment of spawning lamprey migration by deploying distributed networks of such systems in the Great Lakes tributary systems.

Methods

Fabrication of FENG-based pressure sensor array. The PPFE film, purchased from Emfit, Corp., contains extrinsic inorganic silicate nanoparticles serving as stress concentrators. When an external in-plane bidirectional tensile stress was applied to the film, micro-cracking was initiated at the vicinity of the silicate nanoparticles and propagated through the stretching directions. High pressure (i.e., 5 MPa)

nitrogen gas was then introduced to expand the internal cracks into micrometer-sized ellipsoid air pockets. A heat setting process at ～100 ℃ was followed to increase the structural stability. Next, pixelated silver electrodes with 500 nm thickness were deposited and patterned by the DC sputtering coater (Hummer X, Anatech, Inc.) on the front of the sensor array while the backside was designed as a common ground. Finally, the sensor array was completed by creating through-hole vias for each sensing pixel using a precision hole puncher.

Fabrication of encapsulated underwater sensing panel. The sea lamprey detecting system consists of a CMOS-based signal processing panel and an underwater pressure sensing panel, connected with a flat ribbon cable. To ensure the flatness of the sensor, all soldering connections were arranged on the bottom side of the PCB sensing panel while the pressure sensor array was attached to the top side with double-sided Kapton tape. By vertically aligning through-hole vias in both the PCB and the sensor array, the electrical wiring can be realized with aluminum wires and copper tapes. The water impermeability was achieved by first spin coating a 200 μm thick PDMS layer with a mixing ratio of 10:1 onto the pressure sensor array. Next, a supporting acrylic plate was attached on the back of the PCB sensing panel with adhesive 3M VHB bonding tapes applied along the four board edges. PDMS solution with the same mixing ratio used in the protective layer was also applied to seal the slits between bonding tapes and the exposed connectors on the front side of the sensing panel. It should be noted that though the PPFE is waterproof due to is sandwich structure, the proposed encapsulation method is still indispensable to protect the Ag electrodes from lamprey's teeth scraping and the PCB from short-circuit in the underwater environment.

Device characterization and data acquisition. In the single-pixel characterization experiment, the positive pressure loading was generated using a computer-controlled stepping motor, which is described in our previous work\cite{cao2019flexible}. The ball screw transmission mechanism is used to translate

the rotary motion to linear displacement which is further converted into linear compressive pressures through four parallelly connected mechanical springs. The actual pressure is monitored by placing a flexible force sensor (A502, Tekscan, Inc.) between the sensor and the rubber indenter. In negative pressure tests, the partial vacuum pressure is provided by a soft suction cup which is connected to a fluidic control board (see Supplementary Fig. 3). The pressure control apparatus consists of a vacuum pump, a set of solenoid valves, and pressure sensors, and a microcontroller-based autotuning proportional-integral-derivative (PID) controller. The V_{oc} and I_{sc} outputs were both measured by the Keithley 2450 source measure unit (SMU). In the animal test, the voltage signals from each pixelated sensing element were evaluated by a reconfigurable embedded chassis with an integrated intelligent real-time controller (cRIO-9075) and two analog input modules (NI 9201) both from National Instruments.

Data availability.

The data supporting the findings of this study is available from the corresponding author on request.

Acknowledgements

Author contributions statement

Y.C. conceived the plan and was in charge of design, experiments, data acquisition, and analysis. H.S. assisted in circuit design, experimental setup, and data gathering. X.T. and N.S. provided general guidance on the research experiments, contributed to the analysis of the results and assisted in manuscript preparation. All authors contributed to discussions and reviewed the manuscript.

Competing interests

The authors declare no competing financial interests.
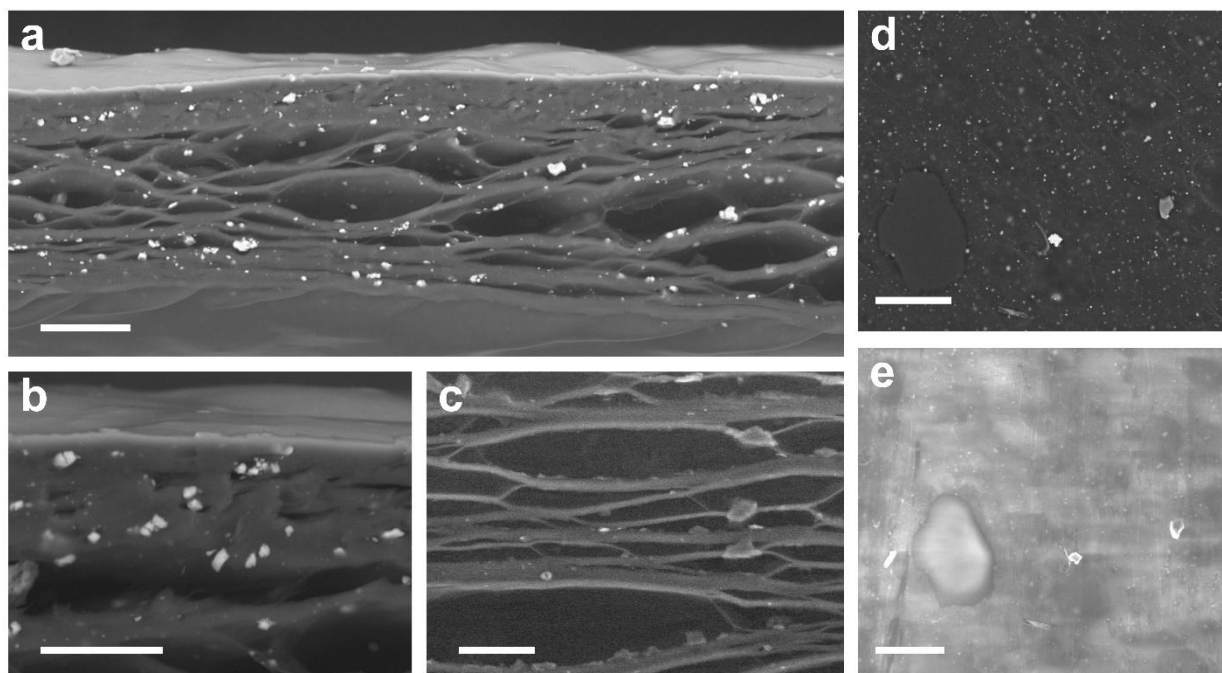
Figure 1 | SEM images of FENG-based pressure sensor. (a) The cross-sectional view of the internal structure of PPFE film, scale bar: 30 μm. **(b)** The close-up view of the continuous PP layer, scale bar: 20 μm. **(c)** The close-up view of the internal macro-scale dipoles, scale bar: 10 μm. **(d)** The top view of the PPFE foam, scale bar: 100 μm. **(e)** The backscattered electron (BSE) image of (d), the darker regions represent the internal ellipsoid voids, scale bar: 100 μm.
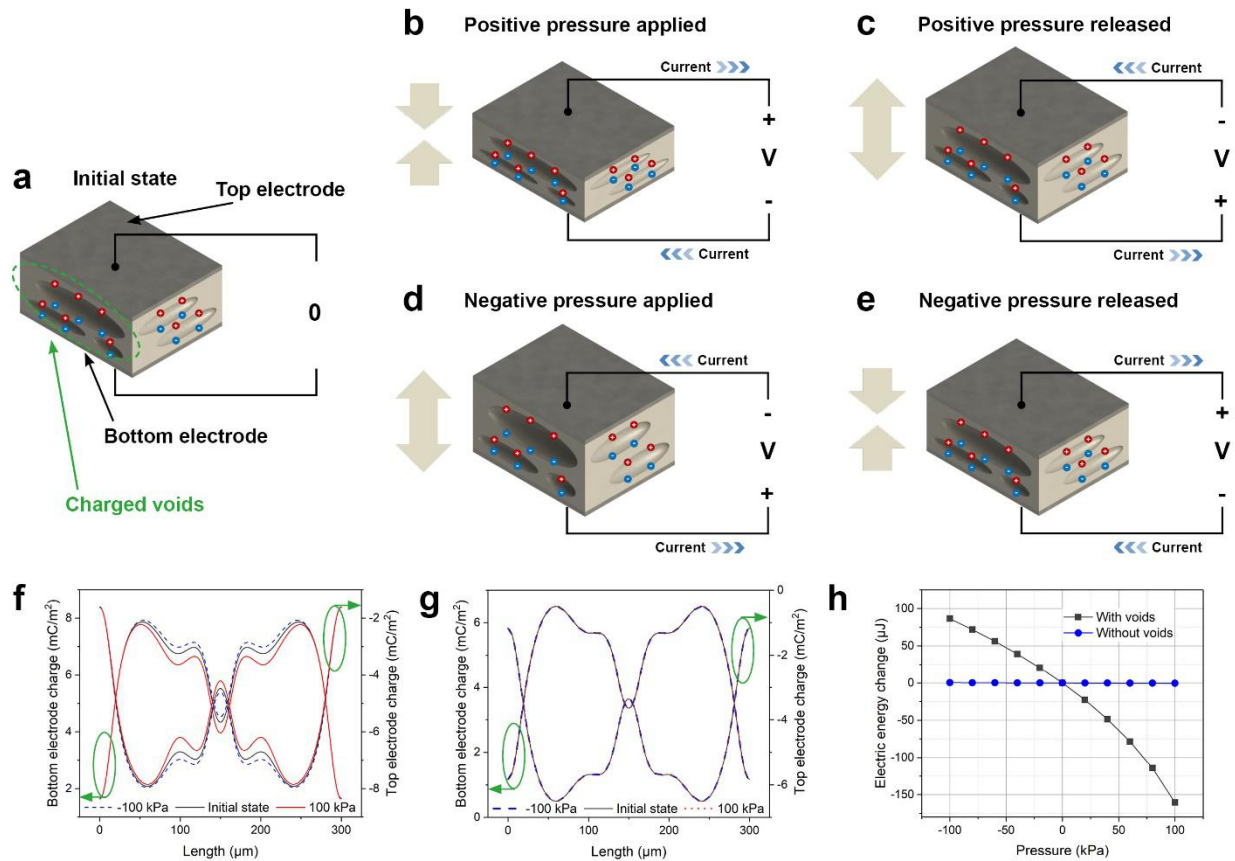

Figure 2 | Working principle of FENG-based pressure sensor. (a) In the initial state of FENG under the unpressured condition, the top and bottom surfaces of the internal air voids are oppositely charged and

form giant dipole moments due to micro-plasma discharging. Mechanoelectrical response of FENG, due to the direct piezoelectric effect, under positive pressure loadings during **(b)** compression and **(c)** releasing processes. **(d, e)** Mechanoelectrical response of FENG when negative pressure loading is applied, the electric outputs show opposite polarities with respect to the signals in the positive loading test. FEM simulation results of surface charge density distributions on the top and bottom surfaces under no pressure, positive pressure, and negative pressure conditions for **(f)** air-voided structure and **(g)** solid structure. **(h)** Comparison of electrical energy converted from mechanical energy for air-voided and solid structures.
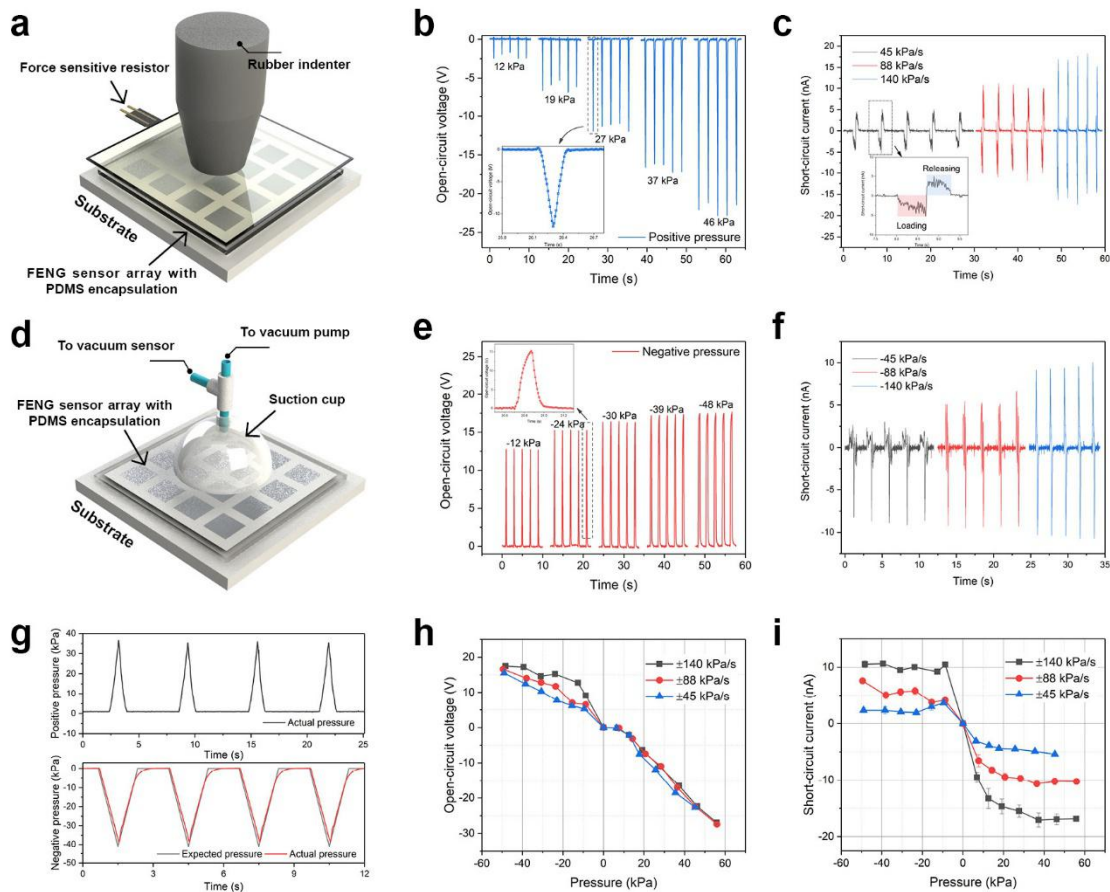
Figure 3 | Characterizations of FENG-based pressure sensor. (**a**) Schematic of the experimental setup for bench test under periodical positive pressure loading. Experimental results under positive pressure loading (**b**) with different pressure amplitudes for V_{oc} measurements and (**c**) with different loading rates for I_{sc} measurements. (**d**) Schematic of the experimental setup for periodical negative pressure loading test. Experimental results under negative pressure loadings (**e**) with different pressure amplitudes for V_{oc} measurements and (**f**) with different loading rates for I_{sc} measurements. (**g**) Waveforms of periodical positive and negative pressures loadings. (**h**) V_{oc} and (**i**) I_{sc} measurements under different pressure amplitudes in the range of -50 to 60kPa at loading rates of 45 kPa/s, 88 kPa/s, and 140 kPa/s, respectively.
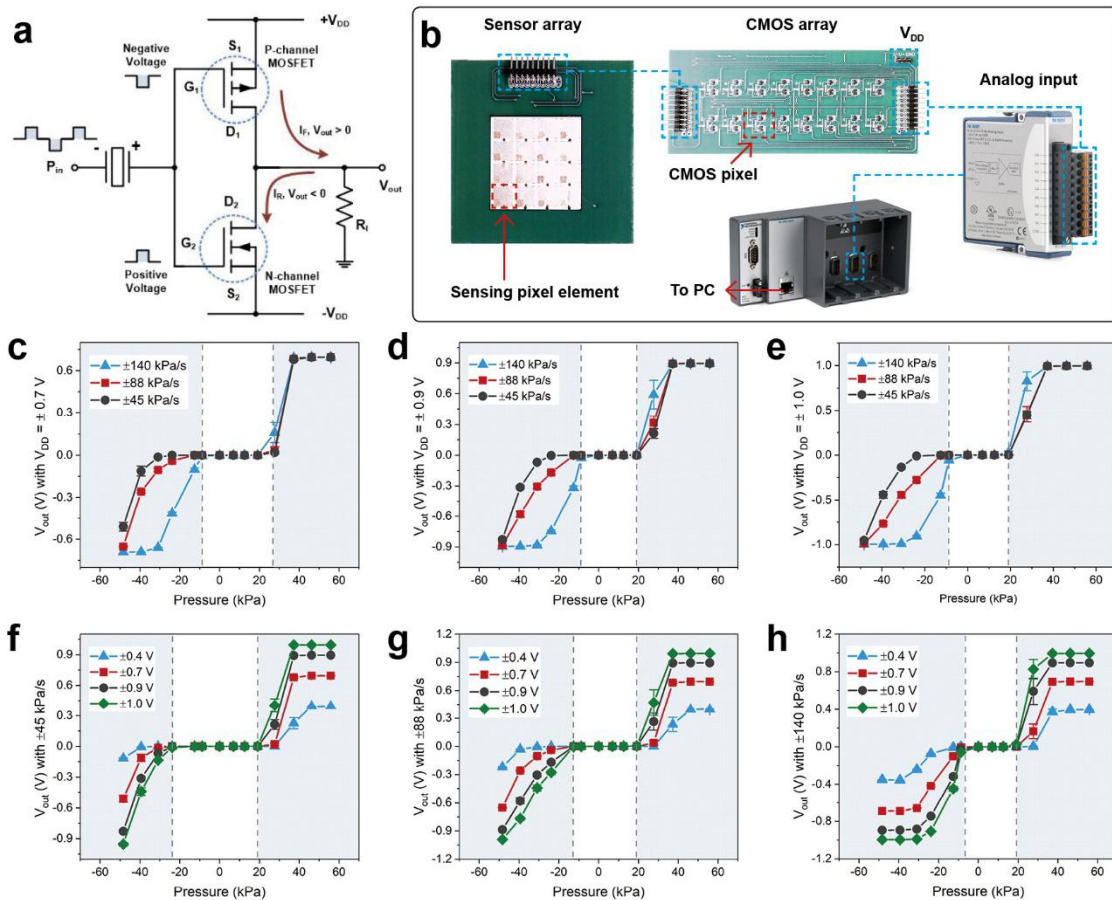
Figure 4 | Characterizations of FENG-based sensor array. (**a**) Schematic of the regulating circuit in each signal processing unit for recognizing positive and negative pressure inputs. (**b**) Illustration of the sea lamprey detecting system and the signal acquisition and processing flow. (**c, d, e**) Regulated output

signal V_{out} under different pressure amplitudes and V_{DD} levels at loading rates of ±45 kPa/s, ±88 kPa/s, and ±140 kPa/s, respectively. **(f, g, h)** Regulated output signal V_{out} under different pressure amplitudes and loading rates at V_{DD} levels of ±0.7 V, ±0.9 V, and ±1.0 V, respectively.
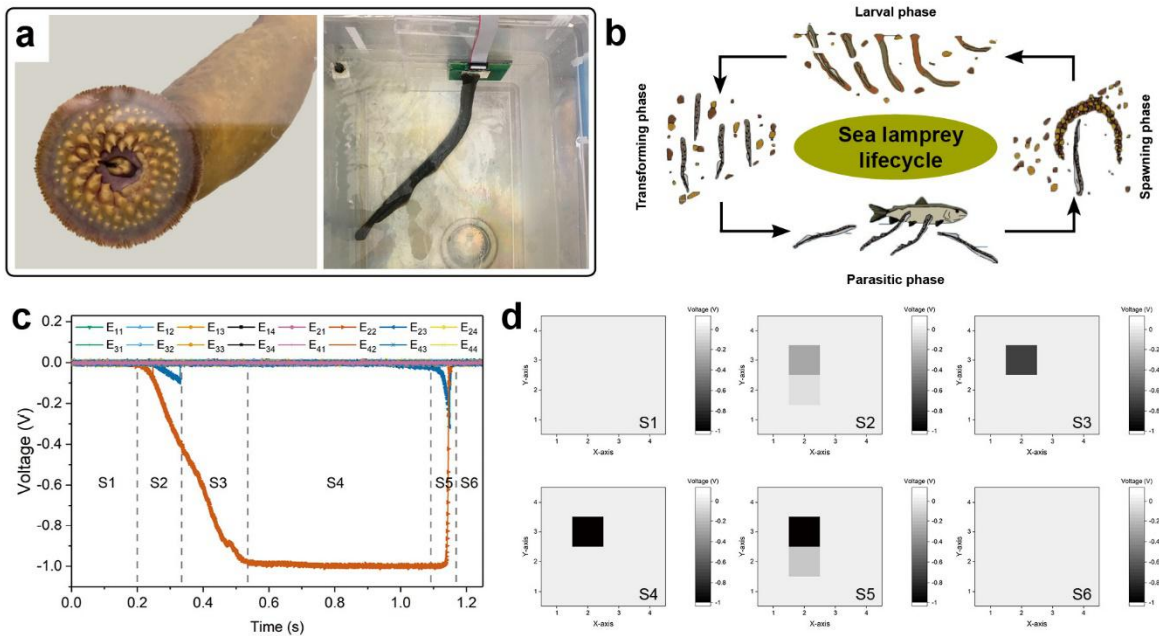
Figure 5 | Demonstration of the potential application in invasive species management. (a) Photographs of an adult sea lamprey with its suction-cup-like mouth and its attachment to the underwater sensing panel. **(b)** Schematic demonstration of the sea lamprey lifecycle. The proposed distributed sensors can be implemented for the invasive lamprey control during the spawning phase. **(c)** Measured suction pressure profiles from each sensing pixel for a full sea lamprey attach-detach cycle on the sensing panel. **(d)** Evolution of the pressure heat map during the 6 suction stages described in (c).

REFERENCES

[1] Smith, B. & Tibbles, J. Sea lamprey (*Petromyzon marinus*) in Lakes Huron, Michigan, and Superior: history of invasion and control, 1936–78. *Can. J. Fish. Aquatic Sci.* 37, 1780–1801 (1980).

[2] Lark, J. G. An early record of the sea lamprey (*Petromyzon marinus*) from Lake Ontario. *J. Fish. Board Can.* 30, 131–133 (1973).

[3] Johnson, N. S., Lewandoski, S. A. & Merkes, C. Assessment of sea lamprey (*Petromyzon marinus*) diet using dna metabarcoding of feces. *Ecol. Indic.* 125, 107605 (2021).

[4] Bryan, M. et al. Patterns of invasion and colonization of the sea lamprey (*Petromyzon marinus*) in North America as revealed by microsatellite genotypes. *Mol. Ecol.* 14, 3757–3773 (2005).

[5] Cuhel, R. L. & Aguilar, C. Ecosystem transformations of the Laurentian Great Lake Michigan by nonindigenous biological invaders. *Annu. Rev. Mar. Sci.* 5, 289–320 (2013).

[6] Docker, M. F. et al. A review of sea lamprey dispersal and population structure in the Great Lakes and the implications for control. *J. Gt. Lakes Res.* 47, S549–S569 (2021).

[7] Miehls, S., Sullivan, P., Twohey, M., Barber, J. & McDonald, R. The future of barriers and trapping methods in the sea lamprey (*Petromyzon marinus*) control program in the Laurentian Great Lakes. *Rev. Fish Biol. Fish.* 30, 1–24 (2020).

[8] Jones, M. L. Toward improved assessment of sea lamprey population dynamics in support of cost-effective sea lamprey management. *J. Gt. Lakes Res.* 33, 35–47 (2007).

[9] Sard, N. M. et al. Rapture (RAD capture) panel facilitates analyses characterizing sea lamprey reproductive ecology and movement dynamics. *Ecol. Evol.* 10, 1469–1488 (2020).

[10] Adams, J. V., Barber, J. M., Bravener, G. A. & Lewandoski, S. A. Quantifying Great Lakes sea lamprey populations using an index of adults. *J. Gt. Lakes Res.* 47, S335–S346 (2021).

[11] Robinson, K. F., Miehls, S. M. & Siefkes, M. J. Understanding sea lamprey abundances in the Great Lakes prior to broad implementation of sea lamprey control. *J. Gt. Lakes Res.* 47, S328–S334 (2021).

[12] Gingera, T. D. et al. Detection and identification of lampreys in Great Lakes streams using environmental DNA. *J. Gt. Lakes Res.* 42, 649–659 (2016).

[13] Schloesser, N. A. et al. Correlating sea lamprey density with environmental DNA detections in the lab. *Manag. Biol. Invasions* 9, 483–495 (2018).

[14] Mize, E. L. et al. Refinement of eDNA as an early monitoring tool at the landscape-level: Study design considerations. *Ecol. Appl.* 29, e01951 (2019).

[15] Zielinski, D. P. et al. Alternative sea lamprey barrier technologies: history as a control tool. *Rev. Fish. Sci. & Aquac.* 27, 438–457 (2019).

[16] Hubbs, C. L. & Pope, T. The spread of the sea lamprey through the great lakes. *Transactions Am. Fish. Soc.* 66, 172–176 (1937).

[17] Shi, H., Holbrook, C. M., Cao, Y., Sepúlveda, N. & Tan, X. Measurement of suction pressure dynamics of sea lampreys, *Petromyzon marinus*. *PLOS One* 16, e0247884 (2021).

[18] González-Afanador, I., Shi, H., Holbrook, C., Tan, X. & Sepúlveda, N. Invasive sea lamprey detection and characterization using interdigitated electrode (IDE) contact sensor. *IEEE Sensors J.* 21, 27947–27956 (2021).

[19] Shi, H., González-Afanador, I., Holbrook, C., Sepúlveda, N. & Tan, X. Soft pressure sensor for underwater sea lamprey detection. *IEEE Sensors J.* 22, 9932–9944 (2022).

[20] Shi, H. et al. Screen-printed soft capacitive sensors for spatial mapping of both positive and negative pressures. *Adv. Funct. Mater.* 29, 1809116 (2019).

[21] Chen, Y. et al. CNT@ leather-based electronic bidirectional pressure sensor. *Sci. China Technol. Sci.* 63, 2137–2146 (2020).

[22] Bai, N. et al. Graded intrafillable architecture-based iontronic pressure sensor with ultra-broad-range high sensitivity. *Nat. Commun.* 11, 1–9 (2020).

[23] Ji, B. et al. Gradient architecture-enabled capacitive tactile sensor with high sensitivity and ultrabroad linearity range. *Small* 17, 2103312 (2021).

[24] Boutry, C. M. et al. Biodegradable and flexible arterial-pulse sensor for the wireless monitoring of blood flow. *Nat. Biomed. Eng.* 3, 47–57 (2019).

[25] Yoo, D., Won, D.-J., Cho, W., Lim, J. & Kim, J. Double side electromagnetic interference-shielded bending-insensitive capacitive-type flexible touch sensor with linear response over a wide detection range. *Adv. Mater. Technol.* 6, 2100358 (2021).

[26] Lin, C.-M., Lin, L.-Y. & Fang, W. Monolithic integration of carbon nanotubes based physical sensors. *In 2010 IEEE 23rd International Conference on Micro Electro Mechanical Systems (MEMS)*, 55–58 (IEEE, 2010).

[27] Atalay, O., Atalay, A., Gafford, J. & Walsh, C. A highly sensitive capacitive-based soft pressure sensor based on a conductive fabric and a microporous dielectric layer. *Adv. materials technologies* 3, 1700237 (2018).

[28] Ruth, S. R. A. et al. Flexible fringe effect capacitive sensors with simultaneous high-performance contact and non-contact sensing capabilities. *Small Struct.* 2, 2000079 (2021).

[29] Zhang, Y. et al. Ferroelectret materials and devices for energy harvesting applications. *Nano Energy* 57, 118–140 (2019).

[30] Cao, Y. & Sepúlveda, N. Design of flexible piezoelectric gyroscope for structural health monitoring. *Appl. Phys. Lett.* 115, 241901 (2019).

[31] Cao, Y., Shi, H., Tan, X. & Sepúlveda, N. Enabling negative pressure sensing through ferroelectret device. *IEEE Sensors Lett.* 6, 1–4 (2022).

[32] Cao, Y., Li, W. & Sepúlveda, N. Performance of self-powered, water-resistant bending sensor using transverse piezoelectric effect of polypropylene ferroelectret polymer. *IEEE Sensors J.* 19, 10327–10335 (2019).

[33] Johnson, N. S., Yun, S.-S., Thompson, H. T., Brant, C. O. & Li, W. A synthesized pheromone induces upstream movement in female sea lamprey and summons them into traps. *Proc. Natl. Acad. Sci.* 106, 1021–1026 (2009).

[34] Johnson, N. S., Snow, B., Bruning, T. & Jubar, A. A seasonal electric barrier blocks invasive adult sea lamprey (*Petromyzon marinus*) and reduces production of larvae. *J. Gt. Lakes Res.* 47, S310–S319 (2021).

[35] Hu, S. et al. Biodegradable, super-strong, and conductive cellulose macrofibers for fabric-based triboelectric nanogenerator. *Nano-micro letters* 14, 1–20 (2022).

[36] Sun, J. et al. Scalable and sustainable wood for efficient mechanical energy conversion in buildings via triboelectric effects. *Nano Energy* 102, 107670 (2022).

[37] Wang, Z. L. Triboelectric nanogenerators as new energy technology for self-powered systems and as active mechanical and chemical sensors. *ACS nano* 7, 9533–9557 (2013).

[38] Wang, H. L., Guo, Z. H., Pu, X. & Wang, Z. L. Ultralight iontronic triboelectric mechanoreceptor with high specific outputs for epidermal electronics. *Nano-micro letters* 14, 1–14 (2022).

[39] Chen, P. et al. Achieving high power density and durability of sliding mode triboelectric nanogenerator by double charge supplement strategy. *Adv. Energy Mater.* 12, 2201813 (2022).

[40] Li, W., Torres, D., Wang, T., Wang, C. & Sepúlveda, N. Flexible and biocompatible polypropylene ferroelectret nanogenerator (feng): On the path toward wearable devices powered by human motion. *Nano Energy* 30, 649–657 (2016).

[41] Cao, Y. et al. Understanding the dynamic response in ferroelectret nanogenerators to enable self-powered tactile systems and human-controlled micro-robots. *Nano Energy* 63, 103852 (2019).

[42] Cao, Y. et al. Flexible ferroelectret polymer for self-powering devices and energy storage systems. *ACS Appl. Mater. & Interfaces* 11, 17400–17409 (2019).

[43] Wan, H. et al. Flexible carbon nanotube synaptic transistor for neurological electronic skin applications. *ACS Nano* 14, 10402–10412 (2020).

[44] Wan, H. et al. Multimodal artificial neurological sensory–memory system based on flexible carbon nanotube synaptic transistor. *ACS Nano* 15, 14587–14597 (2021).

[45] He, J. et al. Recent advances of wearable and flexible piezoresistivity pressure sensor devices and its future prospects. *J. Materiomics* 6, 86–101 (2020).

[46] Li, J., Bao, R., Tao, J., Peng, Y. & Pan, C. Recent progress in flexible pressure sensor arrays: from design to applications. *J. Mater. Chem. C* 6, 11878–11892 (2018).

[47] Gupta, S., Yogeswaran, N., Giacomozzi, F., Lorenzelli, L. & Dahiya, R. Touch sensor based on flexible ALN piezocapacitor coupled with MOSFET. *IEEE Sensors J.* 20, 6810–6817 (2019).

[48] Hahn, C. M. et al. Characterization of a novel hepadnavirus in the white sucker (Catostomus commersonii) from the Great Lakes region of the United States. *J. Virol.* 89, 11801–11811 (2015).

[49] Wang, N. et al. All-organic flexible ferroelectret nanogenerator with fabric-based electrodes for self-powered body area networks. *Small* 17, 2103161 (2021).

[50] Oh, H., Yi, G.-C., Yip, M. & Dayeh, S. A. Scalable tactile sensor arrays on flexible substrates with high spatiotemporal resolution enabling slip and grip for closed-loop robotics. *Sci. Adv.* 6, eabd7795 (2020).

[51] Fissette, S. D. et al. Progress towards integrating an understanding of chemical ecology into sea lamprey control. *J. Gt. Lakes Res.* 47, S660–S672 (2021).

[52] Lin, W. et al. Skin-inspired piezoelectric tactile sensor array with crosstalk-free row+ column electrodes for spatiotemporally distinguishing diverse stimuli. *Adv. Sci.* 8, 2002817 (2021).

Supplementary Information

Yunqi Cao[1], Hongyang Shi[2], Xiaobo Tan[2], and Nelson Sepúlveda[2]

[1]State Key Laboratory of Industrial Control Technology, College of Control Science and Engineering, Zhejiang University, Hangzhou, Zhejiang 310027, China
[2]Department of Electrical and Computer Engineering, Michigan State University, East Lansing, Michigan 48824, United States
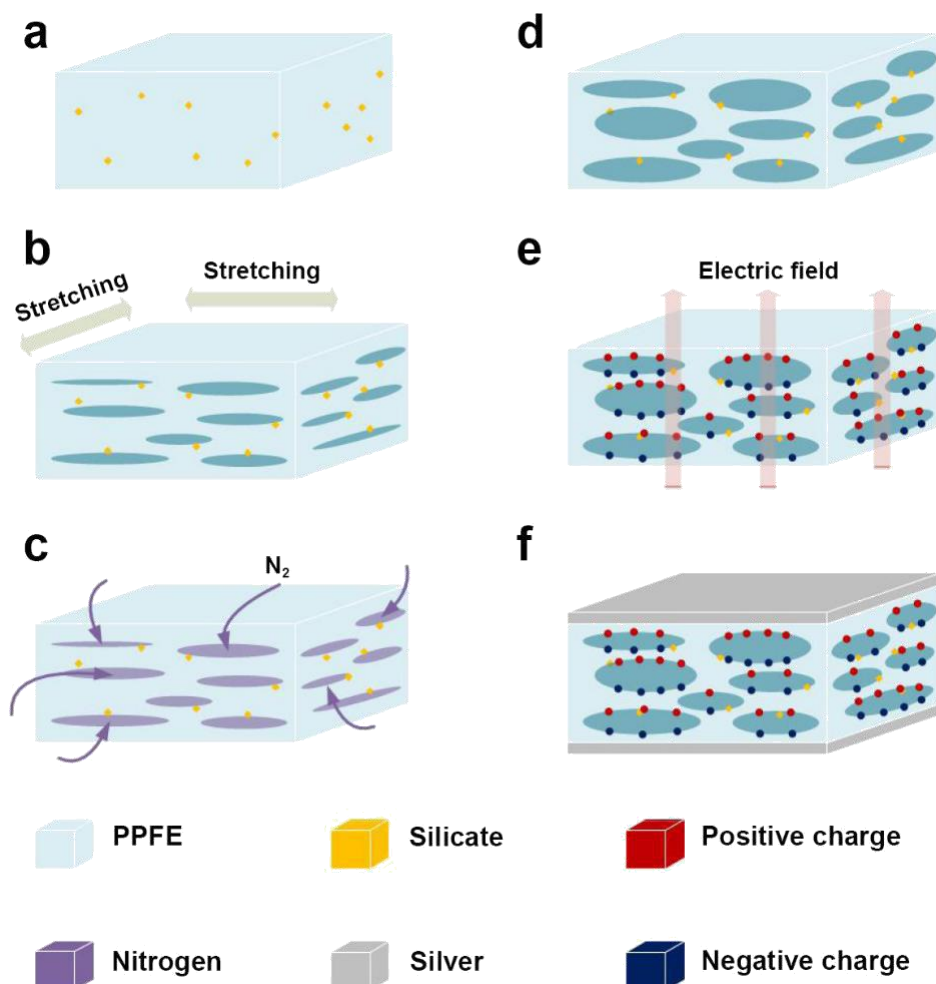
Supplementary Figure 1. Schematic illustration of the device fabrication process. (a) Silicate nanoparticles as stress raisers dispersed in the polypropylene film. (b) In-plane bidirectional stretching is applied to the film, causing micro-cracks initiated in the vicinity of the silicates and propagate along with the stretching directions. (c) High pressure nitrogen gas is introduced and diffuses into the micro-cracks. (d) Release of the high-pressure environment, which allows the micro-cracks to expand into ellipsoidal air voids. (e) High electric field is applied across the film thickness direction, leading to plasma discharging in the air voids and the formation of the giant dipoles. (f) Sputtering coating of top and bottom silver thin films to form metal electrodes.
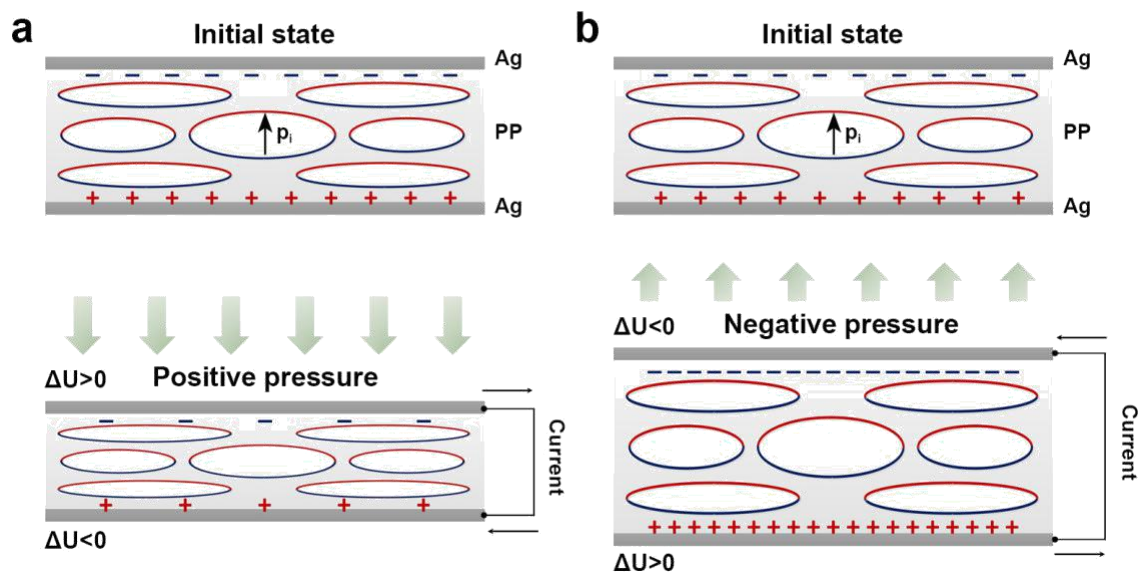
Supplementary Figure 2. Schematic illustration of the transduction working principle under positive and negative pressures. (a) When a positive pressure (compressive load) is applied to the film, induced charge density (σ_e) at top and bottom Ag/PP interfaces decreases due to the decrease in dipole moments, which corresponds to the positive and negative potential change ΔU on top and bottom electrode, respectively. (b) When a negative pressure (partial vacuum) is applied to the film, induced charge density (σ_e) at top and bottom Ag/PP interfaces increases due to the increase in dipole moments, which corresponds to the negative and positive potential change ΔU on top and bottom electrode, respectively.
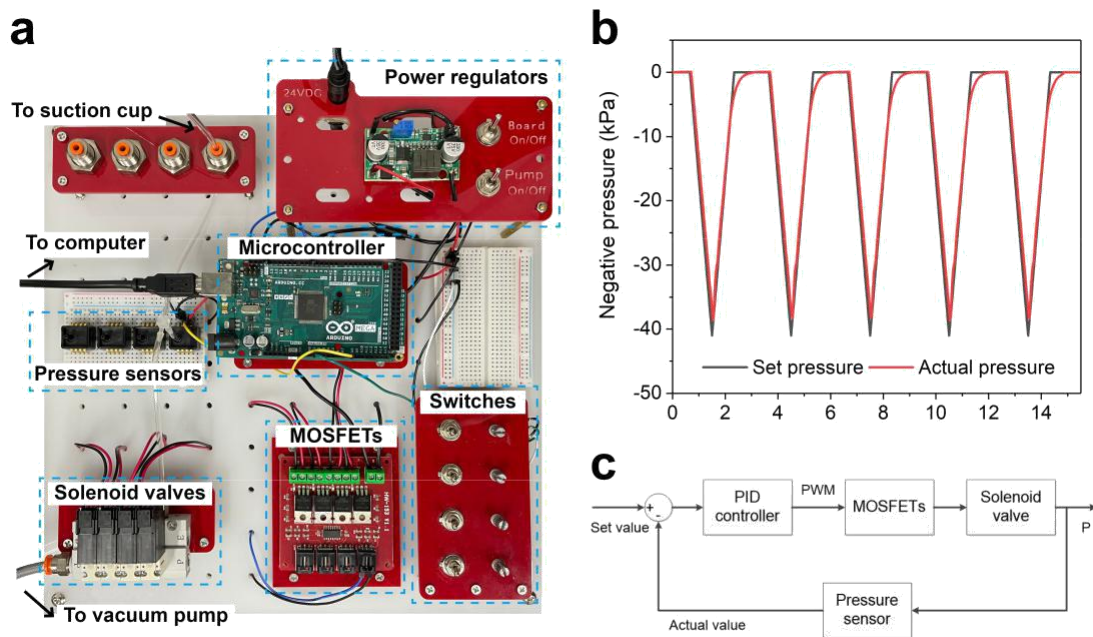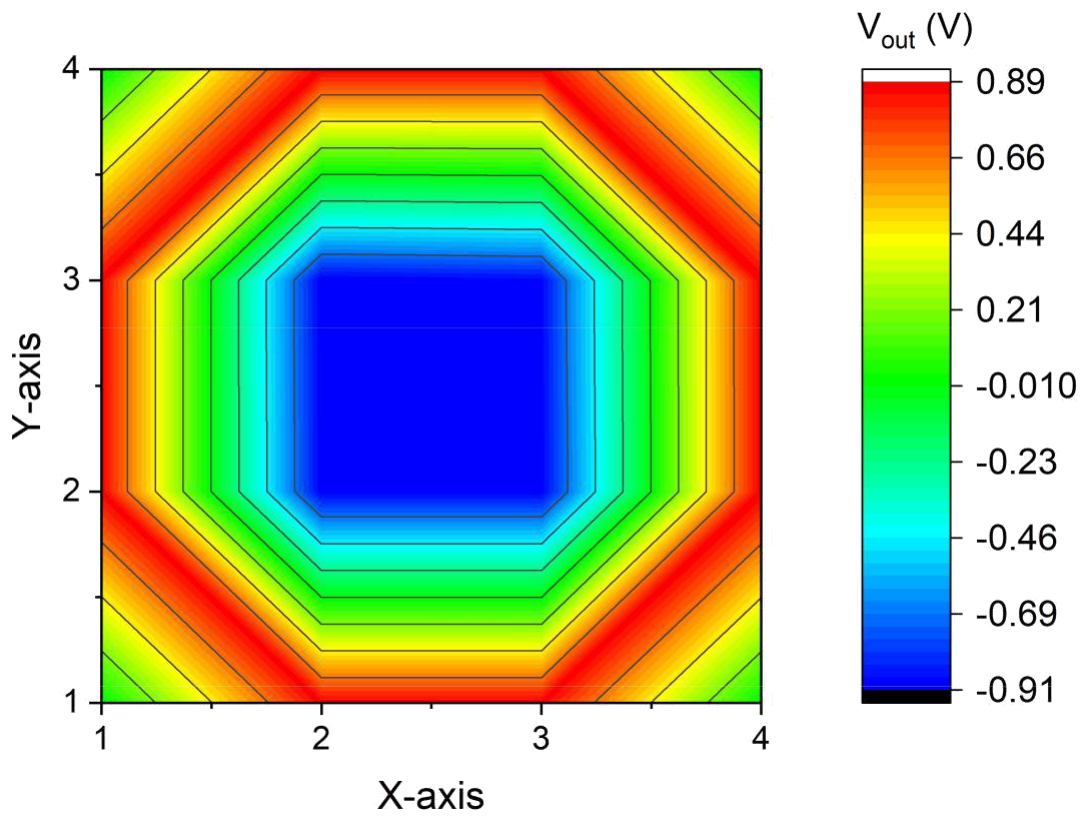
Supplementary Figure 3. Experimental setup of the pneumatic fluidic control system to generate negative pressures. (a) Photograph of the pneumatic fluidic control system including microcontroller, solenoid valves, power regulators, and pressure sensors. (b) Waveform of generated negative pressures where both the loading rate and loading amplitude can be adjusted. (c) Proportional–integral–derivative (PID) control logic of the pneumatic system.
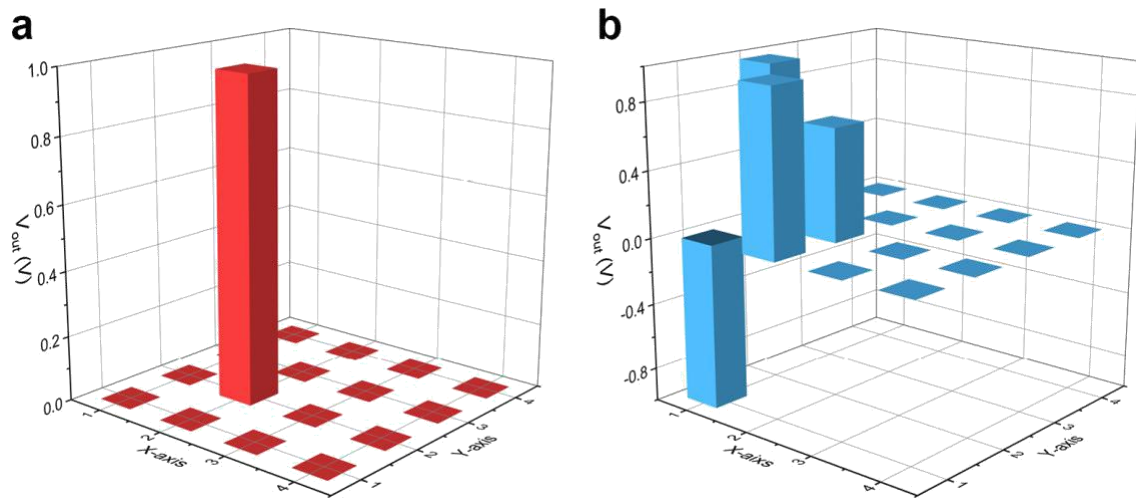
Supplementary Figure 4. Experimental demonstration of cross-talk-free sensor responses under positive and negative pressures. (a) Electric response of the sensing system when only one sensing pixel is activated under a positive pressure while other pixels remain unactivated. (b) Electric response of the sensing system when part of the sensing panel is activated under negative pressure. Since the negative pressure is provided by a suction cup, which has a broad rim margin exerting positive pressures on the sensing panel, the activated area shows both positive and negative pressure responses. This also demonstrates that the sensing system is able to detect both positive and negative pressures.
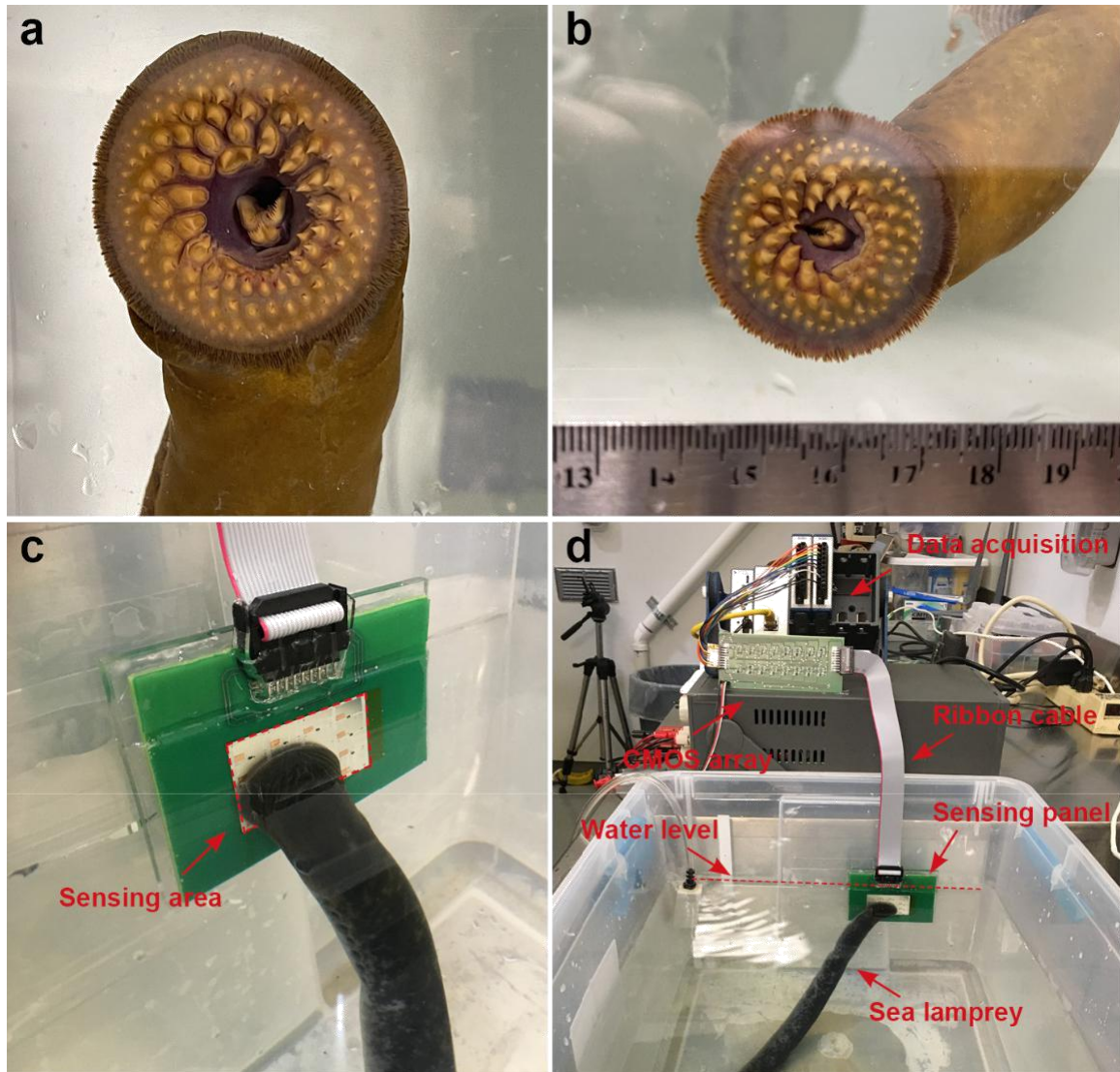
Supplementary Figure 5. Demonstration of sea lamprey detection in an underwater environment using the proposed sensing system. (a) Close-up view of the sea lamprey attaching on the glass window in a water tank. (b) Close-up view of the sea lamprey suction mouth with estimated oral disc diameter of 3 cm. (c) Photo of sea lamprey attaching onto a sensing panel in an underwater environment. (d) Experimental detection of underwater sea lamprey suction pattern using the proposed sensing system, which consists of a water-proof FENG-based sensing panel, a CMOS array, and data acquisition equipment.

Supplementary Figure 6. Experimental demonstration of simultaneous detection of both positive and negative pressures generated by a suction cup using a FENG-based 4 × 4-pixel sensor array.
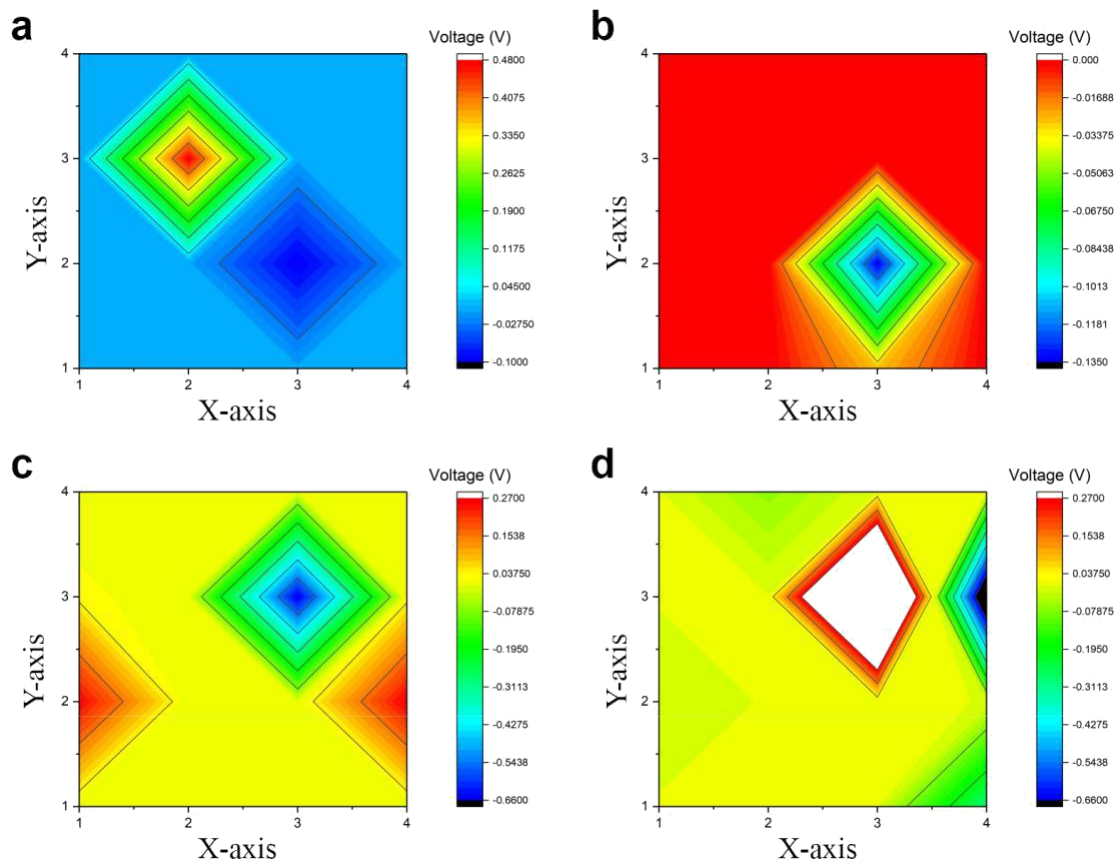
Supplementary Figure 7. The pressure distribution, in terms of output voltage, of adult sea lampreys attaching to different locations of the sensing panel.